DAS recordings of guided waves generated by perforation shots and propagating in a shale reservoir

Ariel Lellouch, Biondo Biondi, Steve Horne, Mark A. Meadows, and Tamas Nemeth

ABSTRACT

We observe distributed acoustic sensing records of guided waves excited by perforation shots in a low-velocity shale layer. Thanks to the high spatial and temporal resolution of distributed acoustic sensing acquisition, unaliased high frequencies of up to 700 Hz can be observed. We analyze and validate the existence of such waves by comparing the recorded data with synthetic data computed using acoustic modeling as recorded in both the horizontal and the vertical segment of the well. These guided waves are trapped within the low velocity organic shale reservoir. Using a simple acoustic-modeling experiment, we show that these waves are sensitive to small velocity changes induced by hydraulic stimulation.

INTRODUCTION

Distributed Acoustic Sensing (DAS) is an emerging technology that allows for high-resolution, continuous recording of the seismic field along an optical fiber (Mateeva et al., 2014; Biondi et al., 2017; Lindsey et al., 2017). DAS is being used in active and passive surveys, both on- and off- shore, in near-surface horizontal trenches as well as in vertical or deviating boreholes (Daley et al., 2016; Dou et al., 2017; Karrenbach et al., 2018). In this study, we analyze perforation shots in a horizontal well recorded on DAS fiber deployed behind casing.

The studied well is located within an unconventional shale layer, which has low velocities and density relative to the surrounding formations. It also exhibits strong anisotropic properties, approximated as VTI. Perforation shots excite waves that propagate through the subsurface and can be measured at distances of up to 500 m on both sides of the source. Through recorded data analysis and synthetic modeling, we demonstrate that the low-impedance shale layer acts as a waveguide. It allows for dispersive propagation of high-frequency (up to 700 Hz) events which are recorded by a DAS array. In applied seismology, guided waves have been previously observed in coal seams and for cross-well tomography (Buchanan, 1976; Krohn, 1992). However, DAS allows for an unprecedented resolution in their analysis. In addition, the high-frequency recording allows for a high sensitivity to small velocity changes, possibly induced by the hydraulic stimulation.

ACQUISITION SETUP AND SUBSURFACE PROPERTIES

In Figure 1a, we show a projection of the trajectory of the well drilled into an unconventional shale layer. The horizontal part of the well spans over 1.5 km in length. In Figure 1b and Figure 1c, we also show velocity and density logs from a vertical well located several hundreds of meters away. The depths of the horizontal and vertical wells have been adjusted. For modeling goals, we modify the log to more realistically match wave propagation. The change is required due to the strongly anisotropic nature of the shale layer. As a result, vertical logging yields much lower velocities than the expected horizontal propagation. The areas of low velocity in the vertical log are related to high shale content, confirmed by a gamma-ray log not shown here. In those areas, we use the velocities estimated from a different sonic log, conducted in the horizontal part of the well depicted in Figure 1a, to partially account for anisotropic effects. Even when taking the horizontal log velocities into account, the velocity of the shale layer is on average less than 4 km/s, whereas the layers above and below it reach velocities of more than 5.3 km/s. We apply some blocking and simplify the modified logs. Resulting velocity and density models, zoomed on the shale layers, are displayed in Figure 1d and Figure 1e. The fiber is installed on the outside of the well casing.

SYNTHETIC EXAMPLE

We first conduct a modeling test using a finite-difference 2D acoustic wave-equation scheme with varying density. Our modeling does not take into account anisotropy, source/receiver directivity, anelastic dissipation, and doesnt represent true (elastic) reflectivity. However, it is fast to compute and can be conducted on a fine grid to model accurately high propagating frequencies. There is no lateral variation in the model. It is based on an extension of the subsurface properties we show in Figure 1d and Figure 1e. The injected source is a zero-phase wavelet with a central frequency of 500 Hz, to emulate high-frequency field records. Two snapshots of the propagating wavefield along with their interpretation are shown in Figure 2. The full modeling extends to depths of roughly 1500 to 2000 m but is not displayed here. The source generates body waves (yellow) which propagate through the subsurface. Because of the velocity structure, head waves also arise after a certain horizontal propagation distance. There are two different modes fast (blue) for the bottom of the shale layer and slow (green) for its top. However, their effect at the location of the horizontal receiver array, positioned within the shale layer, is limited, especially for the fast head wave.In other words, they propagate on the top and bottom of the shale layer but only weakly penetrate it. The guided wave train (shaded in brown) appears clearly at longer propagation distances (right panel). Note its dispersive nature (low frequencies propagate faster) and complex interference patterns. It is clear that the velocity structure enables the propagation of dispersive guided waves that propagate through the shale layer.

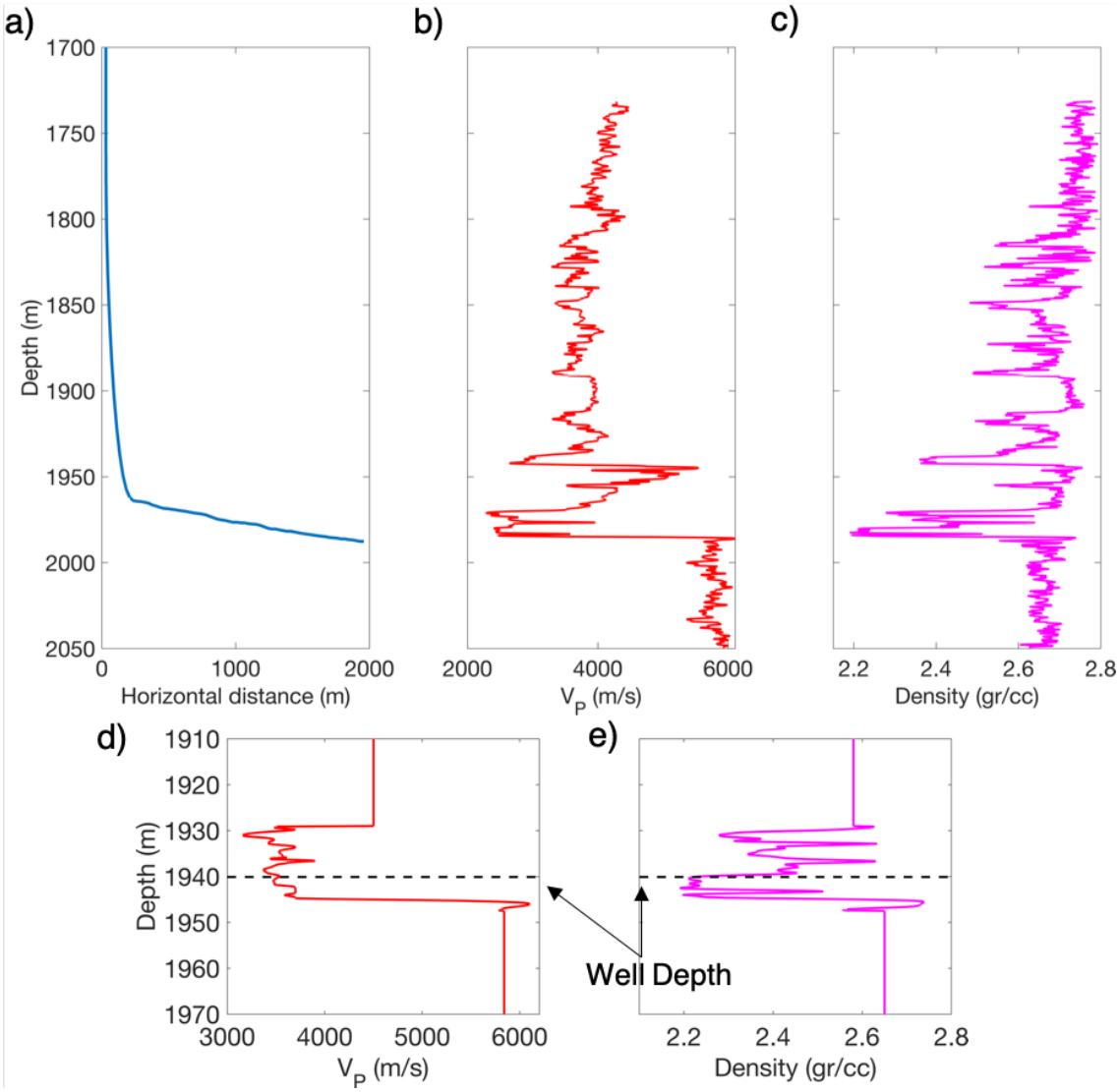

Figure 1: (a) Well trajectory projection. The DAS fiber is deployed all along the well. (b) P-wave sonic log along vertical well located several hundred meters away. (c) Density log along same vertical well. (d) Velocity and (e) density used for modeling, zoomed in on the shale area. Constant velocity and density are used above and below the displayed section. Both source and receivers are located at the black dotted line depth, indicated by arrows. [**NR**]

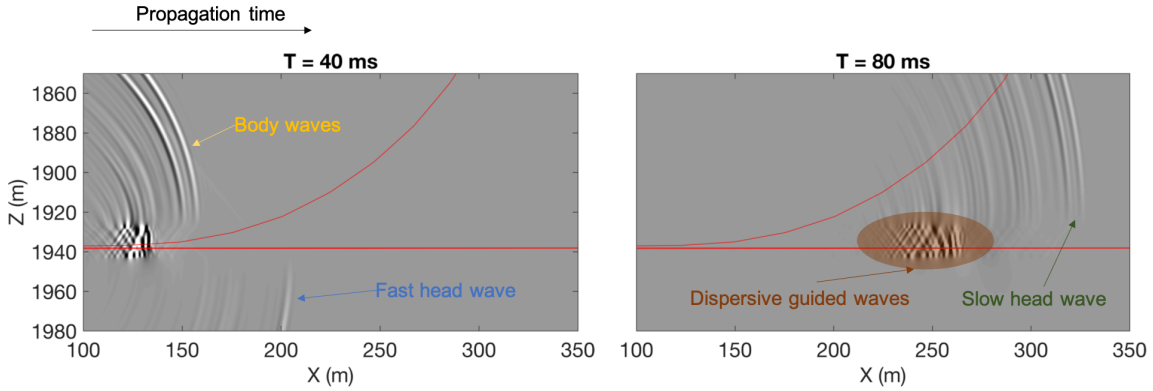

Figure 2: Two snapshots of simulated acoustic wave propagation at 40 ms and 80 ms after source activation, and zoomed on the shale layer. We display two recording arrays (red lines) from which data are extracted for analysis. One is a horizontal array and the other represents the well trajectory near its heel. We denote body waves (yellow), head waves (fast blue, slow green) and guided waves (brown). [**NR**]

FIELD DATA COMPARISON

In this section, we compare recorded field data with the synthetic modeling results. For the field data, a perforation source is recorded along the DAS array. Both source and displayed receivers are in the horizontal part of the well and can be treated as being at the same depth level. Field DAS measurements have a 1 m spacing and 2000 Hz sampling frequency. Due to strong tube waves, we apply an automatic velocity muting to the field data record, computed with a fixed 1500 m/s linear velocity. Our field DAS records display strain rate and are influenced by gauge length effects (Dean et al., 2017). In order to conduct a proper comparison, we first scale synthetic data by a factor of k^2/ω with k being the spatial wavenumber and ω the temporal frequency to convert from pressure to strain-rate. Then, we apply a spatial average of 10 m, which is the field data gauge length, to the synthetic dataset. Finally, we apply a frequency bandpass to the synthetic data to match the frequency range of the field data.

In Figure 3, we show the comparison in both the time (Figure 3a and Figure 3b) and F-K (Figure 3c and Figure 3d) domains. Both datasets contain mostly dispersive guided-wave energy. The synthetic data appear to contain several modes, with different dispersion relations, whereas the field data display only a single mode. When comparing the first mode, we observe that the dispersive behavior is very similar. By F-K analysis not shown here, we find that the phase velocities are, on average, about 10% higher than group velocities. Another difference is the relative strength of a head wave clearly seen in the field data. Such waves are barely visible in the modeled data, as head waves do not radiate deep enough into the shale layer. However, such effects are very sensitive to local geology as well as the exact location of the fiber within the layer. As a supporting argument, the field data do not contain

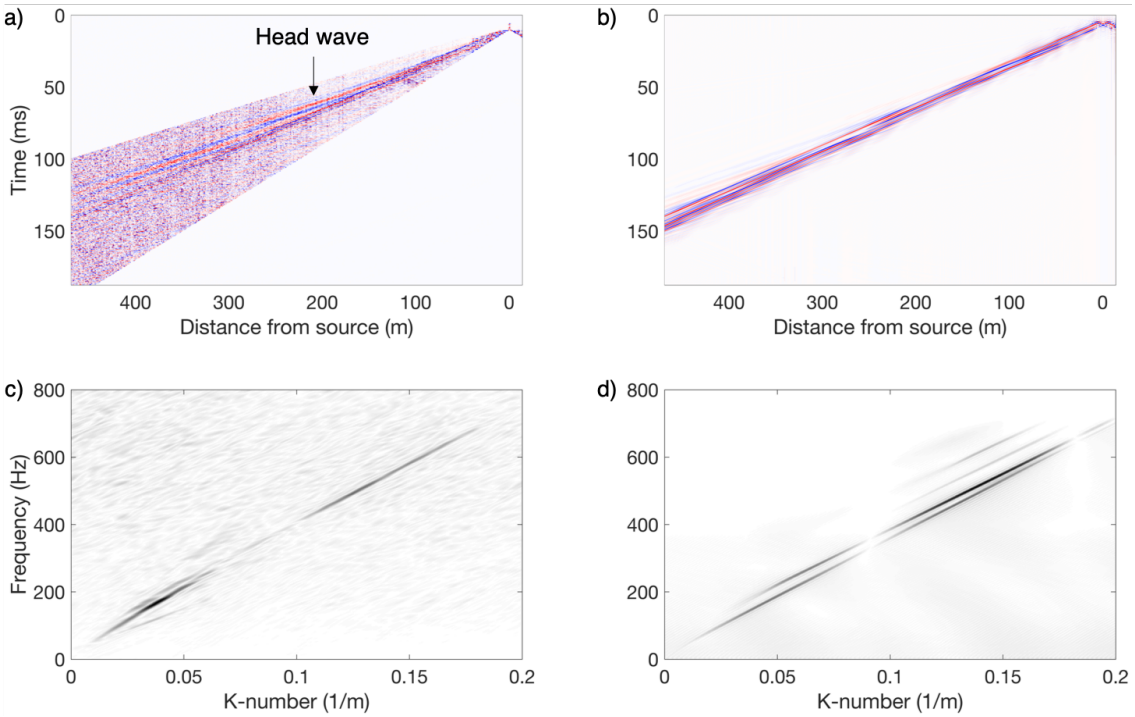

Figure 3: Comparison between field and modeled data. Time-domain field (a) and modeled (b) data. Their F-K spectrum is also shown for field (c) and synthetic (d) data. We observe a strong correlation between the two datasets. The dispersive guided waves are visible in both (c) and (d). In the modeled data, several dispersion modes are present, whereas only a single mode exists for the field data. However, when comparing the same mode, field and modeled data appear to have a similar dispersion curve. The main difference between modeled and field data is the relative strength of the head wave, denoted by a black arrow, in (a). For the field data, a stronger slow head-wave event (black arrow), originating from the top of the shale is present. [**NR**]

the bottom head wave from the very fast (> 5.5 km/s) bedrock, despite a stronger impedance contrast than the one at the top of the formation.

RECORDING IN HORIZONTAL AND VERTICAL PARTS OF THE WELL

Figure 4 shows recordings of a perforation shot in both the horizontal and deviated parts of the well. For the field data (Figure 4b), we display a perforation shot that is close to the wells heel. For the synthetic example (Figure 4a), we extract the wavefield at receiver locations that match the true well trajectory (as shown in Figure 2). The kinematics of the first arrival of the two datasets seem to be in good agreement. This has previously been shown for the horizontal part (right side of the plots), albeit for

a different field record. Despite a very approximate velocity model used for synthetic data generation, the kinematics of the first arrival in the modeled data are consistent with the ones in the field data also in the curving part of the well. Both records show a clear moveout change when the well bends upward (denoted by red arrows). In addition, the guided waves disappear after that location. This critical point occurs at the spatial location where the well exits the shale formation. The propagation velocity is now that of the surrounding medium and not the shale layer. Thus, the apparent velocity is higher. In addition, since receivers are not in the shale layer, guided waves are not present in the record. This is another strong indication that the waves we are analyzing are indeed guided waves propagating in the shale layer. Another interesting feature in the field data recorded in the deviated well section is the presence of significant S-wave energy (denoted by a blue arrow). It follows a different moveout pattern than the P-waves, indicating varying V_P/V_S . The relative strength of the S-waves is due to the fiber directivity, which is more sensitive to S-wave polarizations than to P-waves in this geometrical setup (Martin et al., 2018). Of course, S-waves are not present in the acoustic modeling results.

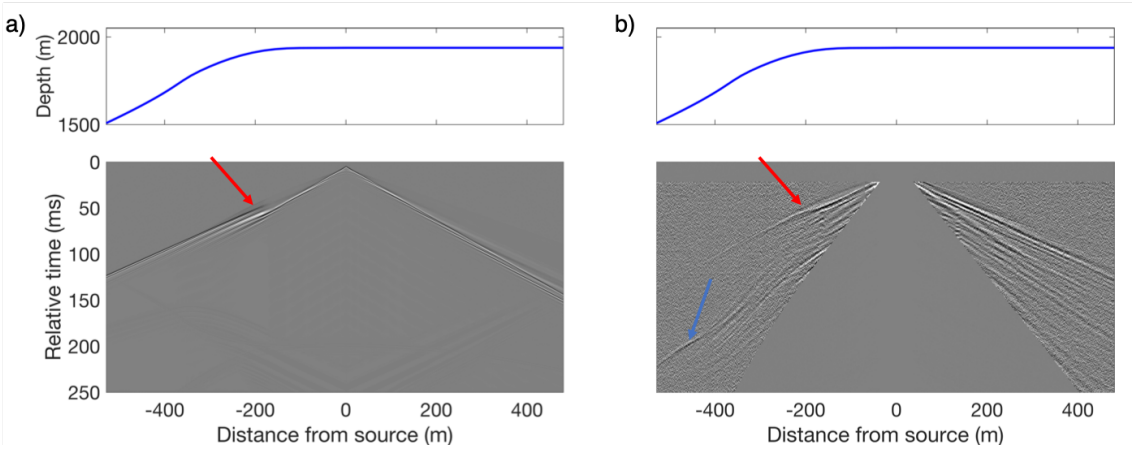

Figure 4: Comparison of synthetic (a) and field (b) records as recorded in both the horizontal and the vertical part of the well. The well depth at each receivers location is displayed as a function of the Euclidean source-receiver offset on top of seismograms. For both cases, propagation towards left (negative distance) indicates receivers in a deviated well while propagation to the right (positive distance) indicates a horizontal acquisition. The traces are displayed with uniform sampling in Euclidean distance between source and receiver points. There is a good kinematic agreement of the recorded phases for the first arrivals. Propagation velocity outside the shale layer is faster, as expected. When the well starts bending (location denoted by red arrows), the guided waves disappear. For the field data record, S-waves (blue arrow) are visible in the vertical part of the well. [**NR**]

SENSITIVITY TO VELOCITY CHANGES

To illustrate the sensitivity of guided waves to velocity variations we show a simple modeling example. It has been shown that hydraulic stimulation causes measurable slowdown in seismic propagation (Binder et al., 2018). In Figure 5, we show a synthetic example of small velocity changes and their effect on recorded guided waves. The velocity model is shown in Figure 5a. The left side of the model is unchanged while the right side is affected by six low-velocity inclusions representative of hydraulic fractures. Each of these is 5 m wide, about 15 m high, and has a 3% velocity and density drop compared to the undisturbed model; such values are significantly smaller than effects reported in Binder et al. (2018).

In Figure 5b, we show two traces recorded at the same distance from the source. After propagation through the disturbed area (red trace), we can observe a 0.25 ms slowdown compared to the background model (blue trace). By taking into account a background propagation velocity of 3700 m/s, a 3% drop over a cumulative 30 m of fractures amounts to a slowdown of 0.25 ms, computed using a simple 1-D horizontal propagation. The recorded wavelet is also slightly distorted. For now, we think that most information lies in propagation velocity changes. Thanks to the high resolution of DAS acquisition, we can measure high-frequency events. Accordingly, smaller travel-time differences, and smaller velocity variations giving rise to them, can be reliably analyzed. In Binder et al. (2018), slowdowns of several milliseconds are observed by VSP data with surface sources. As we measure an approximately tenfold higher frequency, we can expect to measure slowdowns of tenths of milliseconds.

CONCLUSIONS

DAS systems enable the recordings of wavefields in producing wells with dense spatial sampling and high-frequency. Thanks to such high-resolution data we can observe guided waves generated by perforation shots in a low-velocity zone, representative of unconventional plays. Our hypothesis is supported by simple 2-D acoustic modeling, which reproduces most features of the recorded data. In addition, by observing records in the bending and vertical parts of the well, we show that the geological structure is the cause of such guided waves. Finally, we show the guided-waves are highly sensitive to velocity changes, mostly thanks to their high frequency content. Overall, we conclude that guided waves are sampling the low-velocity shale reservoir at a very high frequency, and as such may be used beneficially for its imaging.

ACKNOWLEDGMENTS

We are thankful to Chevron Energy Technology Company for providing recorded data, logs, additional information relevant to this study, and the permission to publish this study. We personally thank Mike Craven and Dimitri Bevc for their helpful comments and discussions.

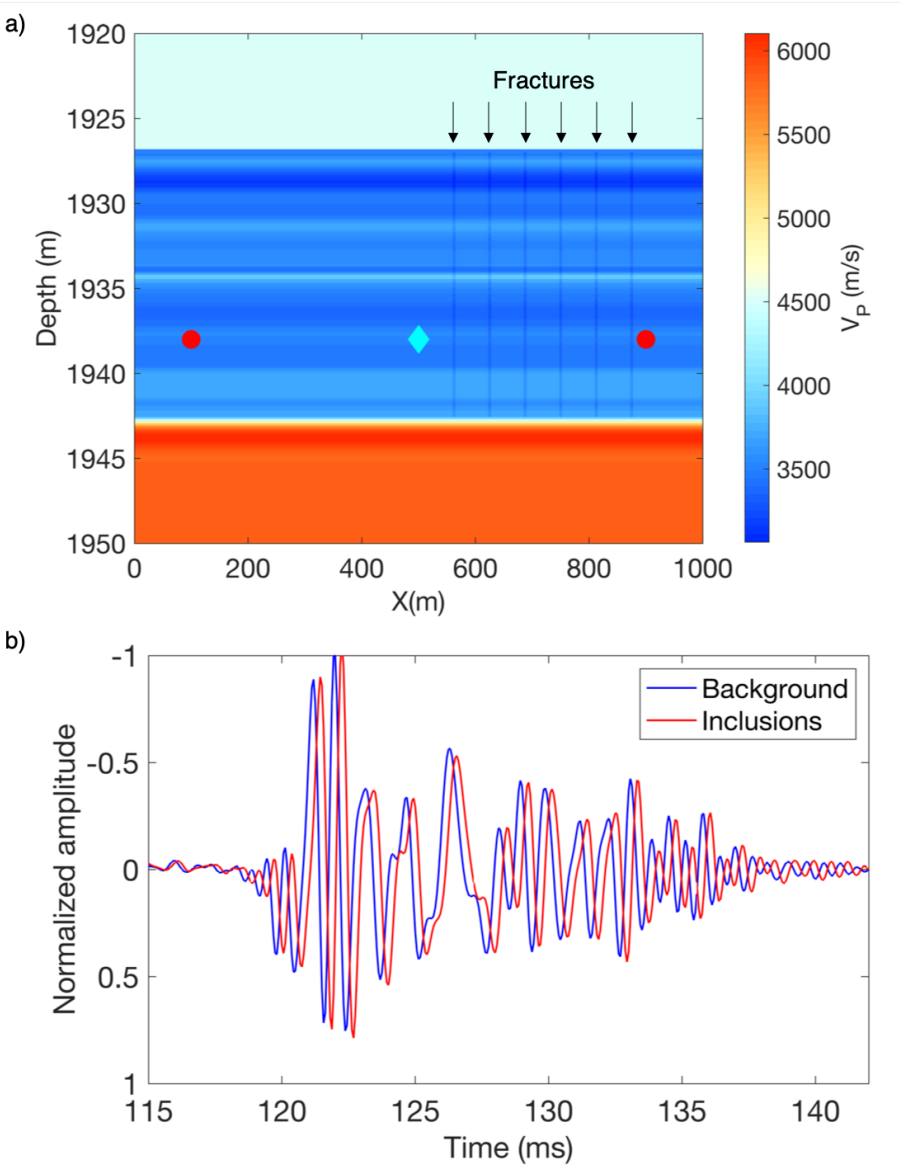

Figure 5: (a) Synthetic test. The layered velocity model from Figure 1 is used as background. While the left side of the model remains unchanged, we add 6 low-velocity zones to the right side. Each of these, denoted by black arrows, is 5m wide, as high as the shale layer (15m) and has a 3% drop in velocity and density. The source (cyan diamond) is excited in the middle of the model and recorded by two receivers positioned at a 400m distance from it (red circles). In (b), we show recorded seimograms at those receiver locations. The seismogram recorded after propagation through the disturbed zones is lagging by about 0.25 ms and the wavelets are slightly distorted. [**NR**]

REFERENCES

Binder, G., A. Titov, D. Tamayo, J. Simmons, A. Tura, G. Byerley, and D. Monk, 2018, Time delays from stress-induced velocity changes around fractures in a time-lapse DAS VSP: SEG Technical Program Expanded Abstracts, 5328–5332.

Biondi, B., E. Martin, S. Cole, M. Karrenbach, and N. Lindsey, 2017, Earthquakes analysis using data recorded by the Stanford DAS Array: SEG Technical Program Expanded Abstracts, 2752–2756.

Buchanan, D. J., 1976, The propagation of attenuated SH channel waves: Geophysical Prospecting, **26**, 16–28.

Daley, T. M., D. E. Miller, K. Dodds, P. Cook, and B. M. Freifeld, 2016, Field testing of modular borehole monitoring with simultaneous distributed acoustic sensing and geophone vertical seismic profiles at Citronelle, Alabama: Geophysical Prospecting, **64**, 1318–1334.

Dean, T., T. Cuny, and A. H. Hartog, 2017, The effect of gauge length on axially incident P-waves measured using fibre optic distributed vibration sensing: Geophysical Prospecting, **65**, 184–193.

Dou, S., N. Lindsey, A. M. Wagner, T. M. Daley, B. Freifeld, M. Robertson, J. Peterson, C. Ulrich, E. R. Martin, and J. B. Ajo-Franklin, 2017, Distributed Acoustic Sensing for Seismic Monitoring of the Near Surface: A Traffic-Noise Interferometry Case Study: Scientific Reports, **7**, 1–12.

Karrenbach, M., S. Cole, A. Ridge, K. Boone, D. Kahn, J. Rich, K. Silver, and D. Langton, 2018, DAS microseismic, strain and temperature monitoring during hydraulic fracturing: Geophysics, **84**, D11–D23.

Krohn, C. E., 1992, Crosswell continuity logging using guided seismic waves: The Leading Edge, **11**, 39–45.

Lindsey, N. J., E. R. Martin, D. S. Dreger, B. Freifeld, S. Cole, S. R. James, B. L. Biondi, and J. B. Ajo-Franklin, 2017, Fiber-Optic Network Observations of Earthquake Wavefields: Geophysical Research Letters, **44**, 792–799.

Martin, E. R., N. J. Lindsey, and B. Biondi, 2018, Introduction to Interferometry of Fiber Optic Strain Measurements: EarthArXiv, **14 June**, 1–33.

Mateeva, A., J. Lopez, H. Potters, J. Mestayer, B. Cox, D. Kiyashchenko, P. Wills, S. Grandi, K. Hornman, B. Kuvshinov, W. Berlang, Z. Yang, and R. Detomo, 2014, Distributed acoustic sensing for reservoir monitoring with vertical seismic profiling: Geophysical Prospecting, **62**, 679–692.